Fault Roughness at Seismogenic Depths and Links to Earthquake Behavior

Elizabeth S. Cochran¹, Morgan T. Page¹, Nicholas J. van der Elst¹, Zachary
E. Ross², Daniel T. Trugman³

5

2

Corresponding author: Elizabeth S. Cochran, ecochran@usgs.gov

¹U.S. Geological Survey, Earthquake Science Center, Pasadena, CA 91106, USA

²California Institute of Technology, Seismological Laboratory, Pasadena, CA 91125, USA

³University of Nevada, Reno, Nevada Seismological Laboratory, Reno, NV 89557, USA

This draft manuscript is distributed solely for the purpose of scientific peer review. Its content is merely being considered for publication, so it is not to be disclosed or released by reviewers. Until the manuscript has been approved for publication by the U.S. Geological Survey (USGS), it does not represent any official USGS finding or policy.

Abstract

Fault geometry affects the initiation, propagation, and cessation of earthquake rupture, as well as, potentially, the statistical behavior of earthquake sequences. We analyze 18,250 events of the 2016-2019 Cahuilla, California swarm and, for the first time, use these high-resolution earthquake locations to map, in detail, the roughness across an active fault surface at depth. We find that the fault is 50% rougher in the slip-perpendicular direction than parallel to slip. 3D mapping of fault roughness at seismogenic depths suggests roughness varies by a factor of 8 over length scales of 1 km. We observe that the largest earthquake (M4.4) occurs where there is significant fault complexity and the highest measured roughness. We also find that b-values are weakly positively correlated with fault roughness. Following the largest earthquake, we observe a distinct population of earthquakes with comparatively low b-values occurring in an area of high roughness values within the rupture area of the M4.4 earthquake. Finally, we measure roughness at multiple scales and find that the fault is self-affine with a Hurst exponent of 0.52, consistent with a Brownian surface.

Introduction

The non-planarity of fault surfaces may control earthquake behavior such as earthquake nucleation, rupture propagation, and slip distribution. Previous studies provide insights into how fault complexity, or roughness, influence earthquake rupture processes. Fang and Dunham (2013) showed through simulations that fault roughness imposed a primary control on local stress heterogeneities as well as the frictional and slip resistance along a fault. Thus, large ruptures tend to start near restraining bends or higher fault complexity that result in a stress asperity (Allam et al., 2019; Lindh & Boore, 1981; Goebel et al., 2012), while similar conditions can cause ruptures to stop in regions where stress conditions preclude continued propagation (Fang & Dunham, 2013). Supershear rupture propagation is more likely to be sustained along geometrically simple fault segments, but transition to supershear rupture velocity is more likely on rough faults (Fang & Dunham, 2013; Bruhat et al., 2016).

The influence of fault geometry on earthquake behavior may be reflected in the magnitude-frequency distributions of earthquake sequences. The Gutenberg-Richter relationship describes the magnitude M distribution of a set of earthquakes N, and is often formulated as: $\log_{10} N \propto -bM$. The parameter b, or b-value, is the slope of the distribution in log-

linear space (Gutenberg & Richter, 1944) and characterizes the relative frequency of larger earthquakes to smaller quakes. While b-values are close to unity on average, variations of b-values in space and over the earthquake cycle have been widely reported (Schorlemmer et al., 2005; Ogata & Katsura, 2014; van der Elst, 2021). Further, laboratory studies have shown that rougher faults may have higher b-values, while lower b-values were observed near geometric asperities that host large slip events (Goebel et al., 2012, 2015, 2017). While laboratory studies show a relationship between the b-value of acoustic emissions and the heterogeneity of the slip surface, it has been considered impossible to observe this correlation in nature (Goebel et al., 2015).

Fault topography or roughness has been inferred from linear surface traces of earth-quake ruptures (e.g., Okubo & Aki, 1987; Wesnousky, 2005) or exhumed fault outcrops (e.g., Power et al., 1987). Recently, fault scanning techniques (LiDAR, laser profilometer, etc) provided high-resolution images across a wide range of length scales of fault surfaces (Sagy et al., 2007; Brodsky et al., 2011; Candela et al., 2011, 2012). These studies confirm the non-planar nature of fault trends and surfaces. Observations of fault corrugation and geometric anisotropy are common, with faults being somewhat smoother in the direction of slip (Power et al., 1987; Sagy et al., 2007; Candela et al., 2011).

While these studies demonstrate that faults deviate significantly from planar surfaces, the observations made on exhumed faults may not provide accurate representations of active faults at seismogenic depths. For example, imaged fault surfaces may be degraded by weathering (Power et al., 1987). Further, due to changing material composition (e.g., soft sediments, greater heterogeneity) and lower confining pressures near the surface, fault geometries may be more complex near the surface and become smoother and simpler at greater depths (Sylvester, 1988). There remains a lack of observations of 3D roughness of seismogenic fault surfaces at depth and imaging the topography of active fault surfaces at sufficient resolution has been beyond the capability of available imaging tools or datasets.

Here, we use a prolific earthquake swarm with well-resolved earthquake locations to probe roughness, for the first time, across an active fault plane at depth and explore its influence on earthquake behavior.

2016-2019 Cahuilla Earthquake Sequence

71

72

73

74

75

76

77

78

79

81

82

85

86

87

88

89

90

91

96

97

99

100

101

102

We study an earthquake swarm near Cahuilla, California that was notable for its productivity, with 18,250 relocated events, and long duration, as it lasted approximately 4 years from early 2016 to late 2019 (Hauksson et al., 2019). The swarm occurred approximately midway between two major fault systems in Southern California, the Elsinore and San Jacinto faults (Figure 1), in a region with numerous, albeit generally smaller swarms (Hauksson et al., 2019; Ross & Cochran, 2021). These swarms are spatially dense, long-duration, and occur ubiquitously in the region between the Elsinore and San Jacinto faults. Their migration patterns suggest they are likely driven by natural fluid migration through the crust at depths of 5-12 km (Ross et al., 2020; Ross & Cochran, 2021).

The Cahuilla swarm, as identified and precisely relocated (38 m and 87 m relative location error in the horizontal and vertical directions, respectively) by Ross et al. (2020), begins at a depth of ~ 7 km and is well-fit by a plane striking 343° and dipping -82°, matching the focal mechanism of the largest event (M4.4) of the sequence. Earthquakes are distributed across much of the fault surface, although with somewhat higher densities in a 500 m-wide zone extending from the presumed injection point up-dip to the top edge of the swarm (Figure 2). The event densities suggest channeling of events along strike away from the high density 'pipe' of events extending up dip from the injection point, similar to channelling inferred from depth histograms by Ross et al. (2020). We use the 10th percentile rupture time in a 150 m by 150 m grid across the fault plane to show the migration of events (Figure 2). Over a period of 4 years the earthquakes migrate approximately 1 km down dip and 3 km up dip, as well as approximately 2 km bilaterally along strike. Events initially migrate steadily for over a \sim 2-year period along strike and dip. However, once earthquakes reach an apparent permeability barrier located approximately 1.75 km up dip from the injection point, migration slows. Then, following the M4.4 mainshock (day 957), rapid migration takes place across the ~ 1 -km wide and 4-km long upper section of the fault.

The M4.4 earthquake occurred following the breach of the inferred permeability barrier (Figure 2) (Ross et al., 2020). Interestingly, stress drops of events above the barrier were reported to be distinctly lower than for the rest of the sequence, perhaps suggesting a difference in the material properties across the barrier (Ross et al., 2020). Waveforms from the M4.4 earthquake were too complex to relocate with waveform cross-correlation

techniques, so we determine the approximate rupture location relative to the relocated catalog using the distribution of earthquakes that occur one day before and after the M4.4 (Figure 1). The estimated rupture area of the M4.4 matches the size of the fault area expected to slip assuming a circular source with a stress drop of 8 MPa, the median value reported for the sequence (Ross et al., 2020).

Methods: 2D and 3D Fault Roughness and b-value

We define fault roughness to be a measure of the deviation from a linear or planar fault surface following Malinverno (1990). This roughness definition subsumes several types of fault complexity including point cloud diffusivity, degree of branching or anastomosing, and fault bending. We first estimate the 2D fault roughness in the alongstrike and along-dip directions. We rotate the data into the fault orientation using the focal mechanism of the M4.4 earthquake (strike 343° , dip -82° , rake 179°). Note the fault rake is 179° , but we assume the fault slip direction is 180° . Then, the fault is divided into a set of along-strike and along-dip profiles using non-overlapping bins every 150 m. We require at least 250 earthquakes to retain the profile. We define the 2D roughness as the mean out-of-profile distance of the earthquakes from the best fit line to the profile.

We also estimate roughness in 3D at all earthquake locations with at least 100 neighboring earthquakes within 500 m. For each roughness estimate, we calculate a best-fit plane using principal component analysis (PCA) for all points within 500 m of the earthquake. The 3D roughness is then estimated as the mean out-of-plane distance from this best-fit plane. The method provides a measure of roughness at a single length scale. We also estimate roughness at multiple length scales, using the same method, in order to measure the roughness scaling exponent.

We estimate b-values using the 'b-positive' method of van der Elst (2021), which uses the positive magnitude differences between successive earthquakes and is robust to transient changes in the completeness. We estimate b-values at the same points where 3D roughness is calculated, but for this calculation we use the nearest 150 $M \geq 0.6$ neighboring earthquakes with positive magnitude differences. Thus, b-values are determined over radii from 400 to 800 m around each point with a median value of 540 m, depending on the density of earthquakes.

Results

The along-strike and along-dip profiles show variable roughness across the fault surface with mean out-of-profile distances between 30 m and 130 m along the \sim 4 km profiles (Figure 3). The along-dip profiles show bends, anastomosing branches, and stepovers, especially towards the SE portion of the rupture. In the along-dip profiles we observe extensive branching and a bend in the fault surface near the location of the inferred permeability barrier (Figure 3). The bend is most prominent along the NW side of the fault and has an amplitude of \sim 500 m out of plane from the remainder of the profile. Near the rupture area of the M4.4 earthquake we observe discontinuities in the fault surface due to both fault branches and step-overs.

The along-strike profiles are more similar to each other in appearance and have a smaller range of mean out-of-plane distances, but also show evidence of complexity. The typical amplitudes of these features in the both along-strike and along-dip profiles are generally less than 200 m, with wavelengths (i.e. along-profile lengths) of about 500 m to 2 km. Overall, the along-dip profiles are 50% rougher than the along-strike profiles, with an average out-of-plane distance of 62 m for the along-dip profiles compared to 43 m for along-strike profiles (Figure 3).

We next extend the analysis to measure complexity across the 3D fault surface. Figure 4A shows the mean out-of-plane distance, or 3D roughness, estimated on the fault for all events within 500 m of an individual earthquake location. We observe that 3D roughness varies by a factor of 8 across the fault surface (0.01 to 0.08 km). The highest roughness values (\sim 80 m) at this length scale are found within the estimated rupture area of the M4.4 earthquake, where the 2D profiles show significant fault complexity. Similar to the 2D profiles, the 3D roughness also shows fault corrugation. The corrugation is oriented sub-parallel-to-oblique to the strike (or rake) direction such that it is somewhat inclined relative to strike from SE to NW. The range of roughness values don't systematically change with depth or along strike.

We similarly explore the distribution of b-values across the fault (Figure 4B). We require 150 positive magnitude differences and impose a magnitude of completeness cutoff ($M_c = 0.6$) to estimate b-values; therefore, b-value estimates sample a range of radii around the earthquake of interest, typically extending 400 to 800 m around each point (the median radius is 540 m). The b-values vary by a factor of ~ 2 (0.8-1.8) across the

fault. The data suggest similar, albeit somewhat weaker, corrugation in b-values as were observed in the 3D roughness. Qualitatively comparing Figure 4A and B, we find that areas of the fault with higher roughness tend to have higher b-values. The exception is in the M4.4 rupture area where we observe the highest roughness values with significant fault branching and bending, but the corresponding b-values are around 1.

We quantitatively compare 3D roughness and b-values for the whole sequence, by plotting roughness and b-value estimates for each earthquake. We compare roughness and b-values before and after the M4.4 in Figure 4C and D. Roughness values pre-M4.4 are between 10–50 m (Figure 4C), while post-M4.4 roughness values are larger (15-110 m) (Figure 4D). Pre- and post-M4.4 b-values are similar, but post-M4.4 b-values have slightly higher maximum b-values (from ~ 1.5 to ~ 1.65). While a weak correlation (correlation coefficient of 0.34) exists between b-value and roughness for the whole sequence (Figure S1), post-M4.4 we note an area of high roughness values with corresponding lower b-values (~ 1.0 -1.2); these anomalous values are primarily within the estimated rupture area of the M4.4 earthquake.

We calculate errors for our roughness and b-value estimates with bootstrapping (resampling the points with replacement, and in the case of the roughness calculation, refitting the plane). 95% confidence bounds on our estimates are shown (for selected points, given that they are highly spatially correlated and overlap) in Figure S1. This plot shows that b-value and roughness estimates in different areas of the fault are distinct given errors due to sample size.

Next, we examine how roughness evolves as events migrate across the fault surface by plotting the roughness values for the whole sequence at the time the event occurred (Figure 4E). We observe an broadening in the range of mean out-of-plane distances through time as more of the fault surface is sampled. Early in the sequence ($_{i}600 \text{ days}$) roughness values are 0.02-0.035 km, expanding to 0.01 to 0.06 km prior to the M4.4 earthquake as the fluid migration continues and we can measure roughness values across a larger fault section. A clear increase in the maximum observed 3D roughness values is observed after the M4.4 earthquake. This increase in mean out-of-plane distance values is due to the high roughness measurements within the inferred rupture area of the M4.4.

We noted above that the <u>distribution of</u> event densities <u>across the fault may suggest</u> shows evidence for fluid channeling (Figure 2A) that could be caused, at least in

part, by may relate to the fault roughness. The orientation and scale of the channeling inferred from the event densities (Figure 2) are similar to the longer wavelength spatial variability in 3D roughness corrugation inferred from the roughness estimates using a radius of 500 m (Figure 4). However, correlation values for event density and roughness (or b-value) are low. This is likely because the total number of events along a section of fault is primarily controlled by the pore pressure change from the natural injection, with the highest event densities in an approximately 1 km wide vertical section above the inferred natural injection point.

We repeat the 3D roughness calculation for a range of radii (125 m to 1.5 km) to determine whether the surface is fractal, and estimate the fractal dimension of the fault surface referred to as the Hurst exponent (e.g. Beeler, 2021). Figure 5 shows the distribution of roughness measurements at different length scales (*i.e.*, twice the radii) as well as their mean and median values. We find the roughness measurements across length scales display power-law behavior, consistent with a self-affine surface, i.e. the surface is self-similar with different scaling factors in the along-strike and along-dip directions. We find a slope (ζ) of 0.52 across length scales from 250 m to 3 km.

Discussion

We explored fault roughness and earthquake behavior across a fault illuminated by a long-duration earthquake swarm near Cahuilla, California. The swarm occurred on a 4 km by 4 km fault at 4 to 8 km depth in low-permeability plutonic rocks (Hauksson et al., 2019). We find evidence for step-overs, fault branching, and corrugation. Corrugation of the fault zone is sub-parallel to the strike direction with a wavelength of approximately 1-2 km and amplitudes typically of a few hundred meters but as large as 500 m. Our observations are similar to those of John (1987) who examined an exposed normal fault system and found corrugations with wavelengths between 0.2-10 km and amplitudes from 30 to 400 m. Examining a smaller fault surface, Sagy and Brodsky (2009) found a broadly undulating fault surface with small (10-40 m), quasi-elliptical bumps protruding \sim 1 m out of the surface. Our data are not of sufficiently high resolution (relative location errors in the 10s of m) to show meter-scale resolution of the fault surface, but confirm the longer wavelength variations in the fault surface.

We also estimate the Hurst exponent (ζ) , or fractal dimension of the surface, to quantify how roughness changes with scale (Candela et al., 2011; Beeler, 2021). Previous studies have generally found surfaces to have Hurst exponents ranging between Brownian and self-similar $(0.5 \le \zeta \le 1)$ (Candela et al., 2012; Beeler, 2021). Here, we find $\zeta = 0.52$ consistent with a Brownian surface. This can be interpreted as the surface being somewhat more correlated over short distances than long distances. Our findings confirm that fault roughness at seismogenic depths is consistent with measurements made using different techniques on rupture traces and exhumed faults.

The distribution of b-values across the fault follows similar spatial patterns as fault roughness. We observe no clear correlation with b-value over the depth range of the sequence (4-8 km). We do find a weak, positive correlation between b-value and roughness with a cross correlation value of 0.34. In laboratory studies, Goebel et al. (2017) suggested that b-values are typically higher on rougher fault surfaces. Simulations have shown that the minimum and maximum magnitudes depend on small scale fault roughness, with shorter wavelength roughness associated with smaller and more numerous earthquakes (Heimisson, 2020). The fault roughness may control the size distribution of earthquakes such that higher roughness is associated with higher b-values, that is, a greater proportion of smaller events. Given the weak correlation observed here, it may be useful to examine b-value and roughness using additional earthquake datasets and simulations.

We find that the largest earthquake (M4.4) occurs in a region with relatively low b-values (1.0-1.2) and corresponding anomalously high roughness (50-80 m) estimates. The correlation between roughness and b-value may break down at higher stressing rates or near asperities where larger events are more likely to occur (Goebel et al., 2012, 2015, 2017). Laboratory studies suggest low b-values correspond to regions where large slip events occur (Goebel et al., 2012, 2015), in agreement with our findings. Larger events observed in the field, laboratory, and simulations are found to preferentially initiate and terminate near fault bends or heterogeneities (Lindh & Boore, 1981; Goebel et al., 2012; Allam et al., 2019). Further, studies have shown that roughness controls the background stress on faults (Fang & Dunham, 2013), nucleation patch size (Okubo & Dieterich, 1984), and maximum magnitude (McLaskey & Lockner, 2014). In the Cahuilla swarm, the high roughness measurement near the rupture area of the M4.4 reflects multiple branches and step-overs and such geometrical heterogeneities may be associated with larger stress (Scholz, 1968; Fang & Dunham, 2013).

We show for the first time that roughness can be measured using a high-resolution catalog of dense earthquake locations along an active fault. As described above, earthquake simulations and laboratory studies show fault roughness controls aspects of earthquake sequences and rupture processes. However, earthquake simulations currently use generic, randomly generated roughness distributions to develop various rupture scenarios. By using high resolution catalogs of small magnitude events to estimate the Hurst exponent and to image fault features including stepovers, branches, and bends, we could provide bespoke geometries and roughness scaling for faults as input into simulations. This could potentially lead to improved forecasting of where earthquakes might start or stop, their slip distributions, and other information important to understanding fault-specific hazard.

Conclusions

We measure roughness of an active fault at depth using earthquake locations from a prolific, multi-year earthquake swarm. We find that the scaling of fault roughness is self-affine and we estimate a scaling exponent (0.52) that is consistent with a Brownian surface. Furthermore, our at-depth roughness measurements are consistent with other measurements of fault roughness estimated from exhumed faults. We find some evidence for a weak correlation between fault roughness and b-value across much of the fault; however, further confirmation of this result from other seismically active areas is needed. Finally, we find that the fault is approximately 50% rougher in the along-dip direction than in the along-strike direction, which is consistent with past observations and the intuition that over time, faults are smoothed in the direction of repeated slip.

Data and Resources

Supplemental Material for this article includes a figure of b-value and roughness for the entire sequence with 95% confidence ranges for selected points, the The Cahuilla swarm catalog is publicly available from the Southern California Earthquake Data Center (https://scedc.caltech.edu/data/cahuilla-swarm.html). All waveform, parametric data, and the conventional catalog are available from the Caltech/USGS Southern California Seismic Network (doi:10.7914/SN/CI) and at the Southern California Earthquake Data Center (doi:10.7909/C3WD3xH1).

Declaration of Competing Interests

The authors declare no competing interests.

Acknowledgments

This work benefited from discussions with Annemarie Baltay, Peter Bird, Emily Brodsky, Tom Hanks, Steve Hickman, and Sarah Minson.

Authors

291

293

- Elizabeth S. Cochran, Morgan T. Page, Nicholas van der Elst, U.S. Geological Survey, Earthquake Science Center, 525 S. Wilson Ave., Pasadena, CA 91106.
- Zachary E. Ross, California Institute of Technology, Seismological Laboratory, 1200
 E. California Blvd., MS 252-21, Pasadena, CA 91125.
- Daniel T. Trugman, University of Nevada, Reno, Department of Geological Sciences and Engineering, 1664 N. Virginia Street, Reno, NV 89557-0172.

References

303

- Allam, A. A., Kroll, K. A., Milliner, C. W. D., & Richards-Dinger, K. B. (2019). Effects of Fault Roughness on Coseismic Slip and Earthquake Locations. *J Geo-*phys Res, 124 (11), 11336–11349. doi: 10.1029/2018JB016216
- Beeler, N. M. (2021). Characterizing fault roughness—Are faults rougher at long or
 short wavelengths? (Open-File Report No. 2020-1134). U.S. Geological Survey.
 (doi: 10.3133/ofr20201134)
- Brodsky, E. E., Gilchrist, J. J., Sagy, A., & Collettini, C. (2011). Faults smooth gradually as a function of slip. Earth Planet Sci Lett, 302(1), 185–193. doi: 10

 1016/j.epsl.2010.12.010
- Bruhat, L., Fang, Z., & Dunham, E. M. (2016). Rupture complexity and the supershear transition on rough faults. J Geophys Res, 121(1), 210-224. doi: 10.1002/2015
- Candela, T., Renard, F., Klinger, Y., Mair, K., Schmittbuhl, J., & Brodsky, E. E.

 (2012). Roughness of fault surfaces over nine decades of length scales. *J Geophy Res*, 117(B8). doi: 10.1029/2011JB009041
- Candela, T., Renard, F., Schmittbuhl, J., Bouchon, M., & Brodsky, E. E. (2011).

 Fault slip distribution and fault roughness. *Geophys J Int*, 187(2), 959–968.

 doi: 10.1111/j.1365-246X.2011.05189.x
- Fang, Z., & Dunham, E. M. (2013). Additional shear resistance from fault roughness and stress levels on geometrically complex faults. *J Geophys Res*, 118(7), 3642–3654. doi: 10.1002/jgrb.50262
- Goebel, T. H. W., Becker, T. W., Schorlemmer, D., Stanchits, S., Sammis, C., Ry-backi, E., & Dresen, G. (2012). Identifying fault heterogeneity through mapping spatial anomalies in acoustic emission statistics. *J Geophy Res*, 117(B3). doi: 10.1029/2011JB008763
- Goebel, T. H. W., Kwiatek, G., Becker, T. W., Brodsky, E. E., & Dresen, G. (2017).

 What allows seismic events to grow big?: Insights from b-value and fault
 roughness analysis in laboratory stick-slip experiments. Geology, 45(9), 815–
 818. doi: 10.1130/G39147.1
- Goebel, T. H. W., Sammis, C. G., Becker, T. W., Dresen, G., & Schorlemmer, D.

 (2015). A comparison of seismicity characteristics and fault structure between

 stick—slip experiments and nature. *Pure Appl Geophys*, 172(8), 2247–2264. doi:

- 336 10.1007/s00024-013-0713-7
- Gutenberg, B., & Richter, C. F. (1944). Frequency of earthquakes in California. *Bull*Seismol Soc Am, 34(4), 185–188. doi: 10.1785/BSSA0340040185
- Hauksson, E., Ross, Z. E., & Cochran, E. (2019). Slow-growing and extended-
- duration seismicity swarms: Reactivating joints or foliations in the Cahuilla
- Valley Pluton, Central Peninsular Ranges, Southern California. J Geophy Res,
- 124(4), 3933-3949. doi: 10.1029/2019JB017494
- Heimisson, E. R. (2020). Crack to pulse transition and magnitude statistics dur-
- ing earthquake cycles on a self-similar rough fault. Earth Planet Sci Lett, 537,
- 345 116202. doi: 10.1016/j.epsl.2020.116202
- John, B. E. (1987). Geometry and evolution of a mid-crustal extensional fault sys-
- tem: Chemehuevi Mountains, southeastern California. Geological Society, Lon-
- don, Special Publications, 28(1), 313–335. doi: 10.1144/GSL.SP.1987.028.01
- .20
- Lindh, A. G., & Boore, D. M. (1981). Control of rupture by fault geometry during
- the 1966 parkfield earthquake. Bull Seismol Soc Am, 71(1), 95–116. doi: 10
- .1785/BSSA0710010095
- Malinverno, A. (1990). A simple method to estimate the fractal dimen-
- sion of a self-affine series. Geophys Res Lett, 17(11), 1953–1956. doi:
- 10.1029/GL017i011p01953
- McLaskey, G. C., & Lockner, D. A. (2014). Preslip and cascade processes initiat-
- $_{357}$ ing laboratory stick slip. J Geophy Res, 119(8), 6323–6336. doi: 10.1002/
- 358 2014JB011220
- ogata, Y., & Katsura, K. (2014). Comparing foreshock characteristics and fore-
- shock forecasting in observed and simulated earthquake catalogs. J Geophys
- Res, 119(11), 8457–8477. doi: 10.1002/2014JB011250
- Okubo, P. G., & Aki, K. (1987). Fractal geometry in the San Andreas Fault System.
- ³⁶³ J Geophy Res, 92(B1), 345–355. doi: 10.1029/JB092iB01p00345
- Okubo, P. G., & Dieterich, J. H. (1984). Effects of physical fault properties on fric-
- tional instabilities produced on simulated faults. J Geophy Res, 89 (B7), 5817–
- 5827. doi: 10.1029/JB089iB07p05817
- Power, W. L., Tullis, T. E., Brown, S. R., Boitnott, G. N., & Scholz, C. H. (1987).
- Roughness of natural fault surfaces. Geophys Res Lett, 14(1), 29–32. doi: 10

- .1029/GL014i001p00029
- Ross, Z. E., & Cochran, E. S. (2021). Evidence for latent crustal fluid injection tran-
- sients in Southern California from long-duration earthquake swarms. Geophysical Scients in Southern California from long-duration earthquake swarms.
- 372 Res Lett, 48(12), e2021GL092465. doi: 10.1029/2021GL092465
- Ross, Z. E., Cochran, E. S., Trugman, D. T., & Smith, J. D. (2020). 3D fault ar-
- chitecture controls the dynamism of earthquake swarms. Science, 368 (6497),
- 375 1357–1361. doi: 10.1126/science.abb0779
- Sagy, A., & Brodsky, E. E. (2009). Geometric and rheological asperities in an ex-
- posed fault zone. J Geophy Res, 114 (B2). doi: 10.1029/2008JB005701
- Sagy, A., Brodsky, E. E., & Axen, G. J. (2007). Evolution of fault-surface roughness
- with slip. Geology, 35(3), 283–286. doi: 10.1130/G23235A.1
- Scholz, C. H. (1968). The frequency-magnitude relation of microfracturing in rock
- and its relation to earthquakes. Bull Seismol Soc Am, 58(1), 399–415. doi: 10
- .1785/BSSA0580010399
- Schorlemmer, D., Wiemer, S., & Wyss, M. (2005). Variations in earthquake-size dis-
- tribution across different stress regimes. Nature, 437(7058), 539–542. doi: 10
- 385 .1038/nature04094
- Sylvester, A. G. (1988). Strike-slip faults. GSA~Bull,~100(11),~1666-1703.~doi:~10
- $.1130/0016-7606(1988)100\langle 1666:SSF \rangle 2.3.CO; 2$
- van der Elst, N. J. (2021). B-positive: A robust estimator of aftershock magni-
- tude distribution in transiently incomplete catalogs. J Geophy Res, 126(2),
- e2020JB021027. doi: 10.1029/2020JB021027
- Wesnousky, S. G. (2005). Active faulting in the Walker Lane. *Tectonics*, 24(3). doi:
- 392 10.1029/2004TC001645

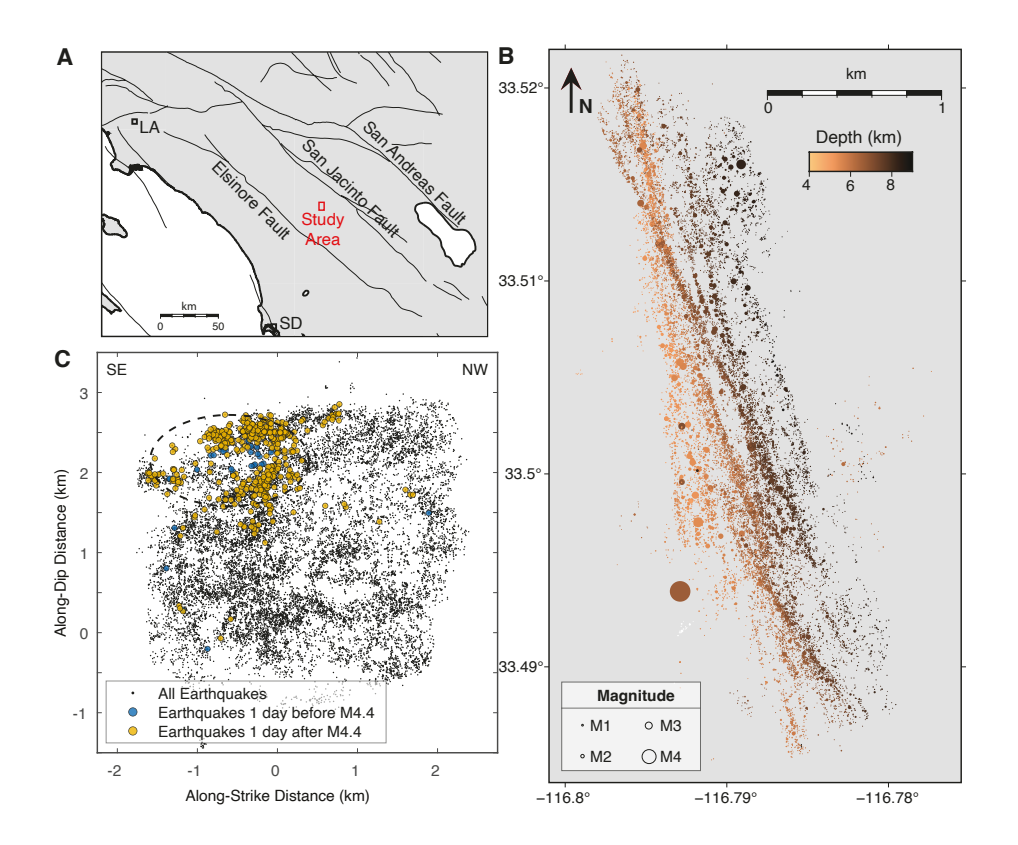


Figure 1. The 2016-2019 Cahuilla earthquake swarm in Southern California. (Top Left) Overview map of the study area (red box) in southern California showing major fault locations (black lines) with the Elsinore, San Jacinto, and San Andreas Faults labeled. The locations of the major cities of Los Angeles (LA) and San Diego (SD), California are shown by black squares. (Right) Map of the earthquakes (filled circles) colored by depth and scaled by magnitude. Legend given at left. Note that for the largest earthquake, a M4.4 shown on the SW portion of the sequence, we show the SCSN catalog location as the event was not relocated by GrowClust. (Bottom Left) Distribution of earthquakes (black dots) in the along-fault orientation, assuming a strike of 343 degrees and dip of -82 degrees inferred from the focal mechanism of the M4.4 mainshock. The origin is set to be the initiation point of the swarm. The approximate location of the M4.4 earthquake (dashed oval) relative to the relocated event catalog is estimated using the earthquakes that occur one day before (blue dots) and after (yellow dots) the M4.4. The size of the oval approximates the fault area expected for a M4.4 earthquake with a stress drop of 8 MPa.

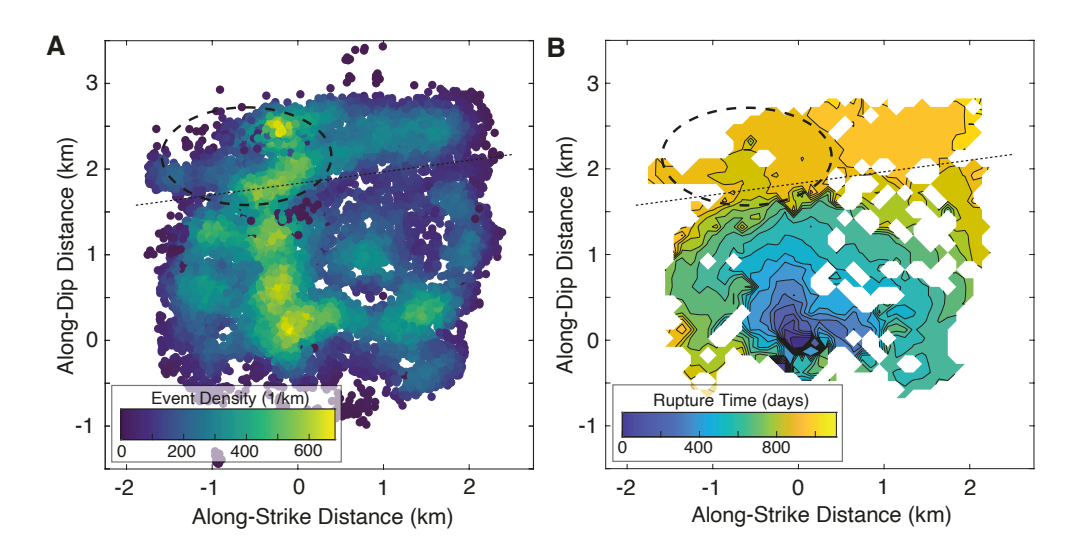


Figure 2. (A) Density of earthquakes across the fault plane, averaged over volumes with a radius of 0.25 km, using earthquakes above the magnitude of completeness (M_c =0.6). The approximate location of the M4.4 rupture area is indicated by the dashed black oval. The approximate location of the permeability barrier inferred from the percentile rupture time plotted in (B) is indicated by the dotted black line. (B) 10th percentile rupture time across the fault plane; annotations are the same as in (A).

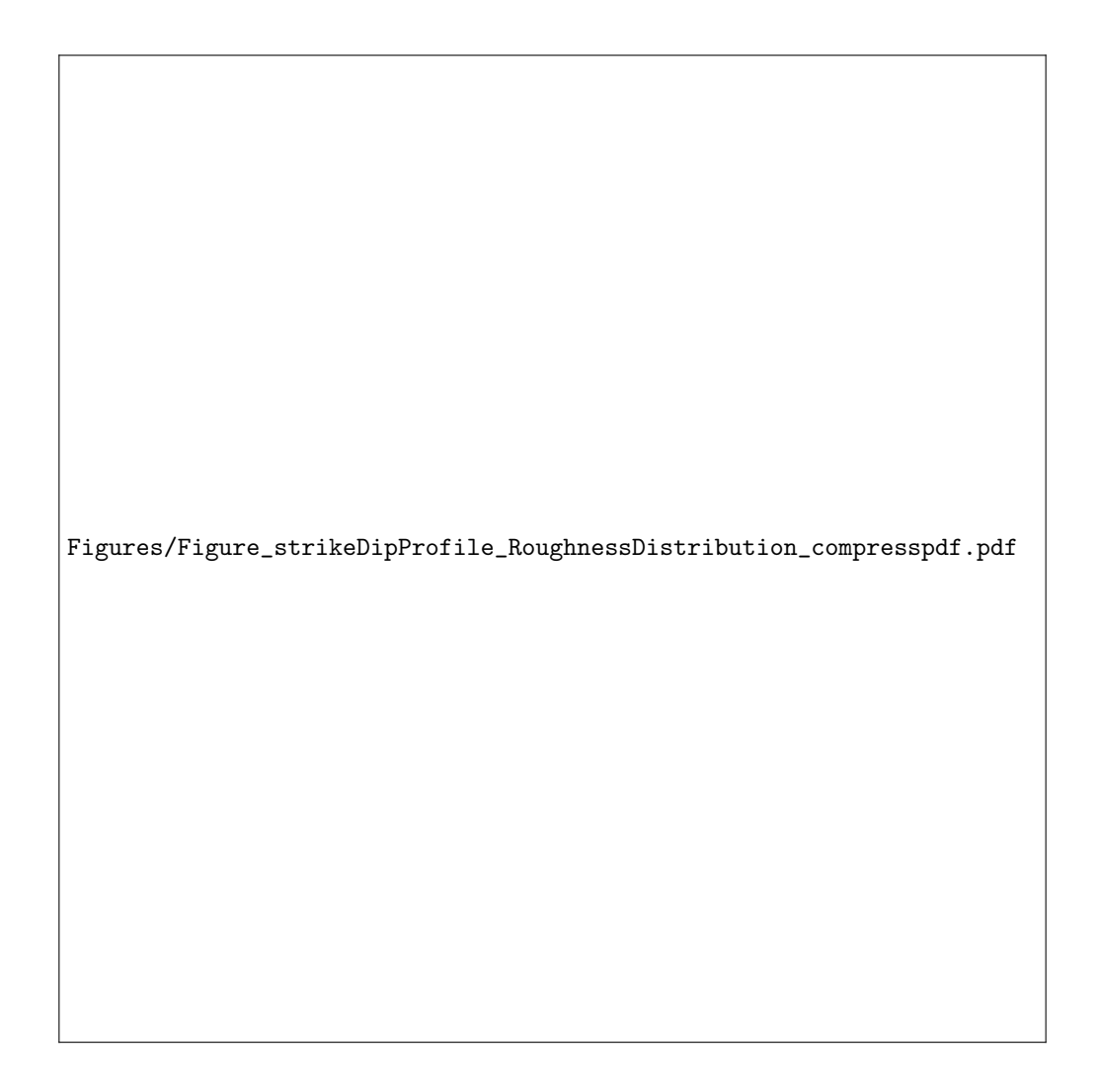


Figure 3. (A) Along-strike (top) and along-dip (bottom) fault profiles for 150-m wide bins. Profiles are colored by the 2D estimate of roughness defined as the mean of the absolute value of residuals to a linear fit to the along-dip or along-strike profile. Only profiles with at least 250 earthquakes are plotted and evaluated. The fault perpendicular distance scale bar is shown in the lower right of each subplot. The approximate location of the M4.4 rupture area is shown by the dashed black rectangles on both profiles and the approximate location of the inferred permeability barrier is shown by the dotted black line on the along-dip profiles plot. (B) Frequency distribution of mean 2D roughness for the along-strike (top) and along-dip (bottom) profiles show that the fault is approximately 50% rougher in the direction parallel to slip.

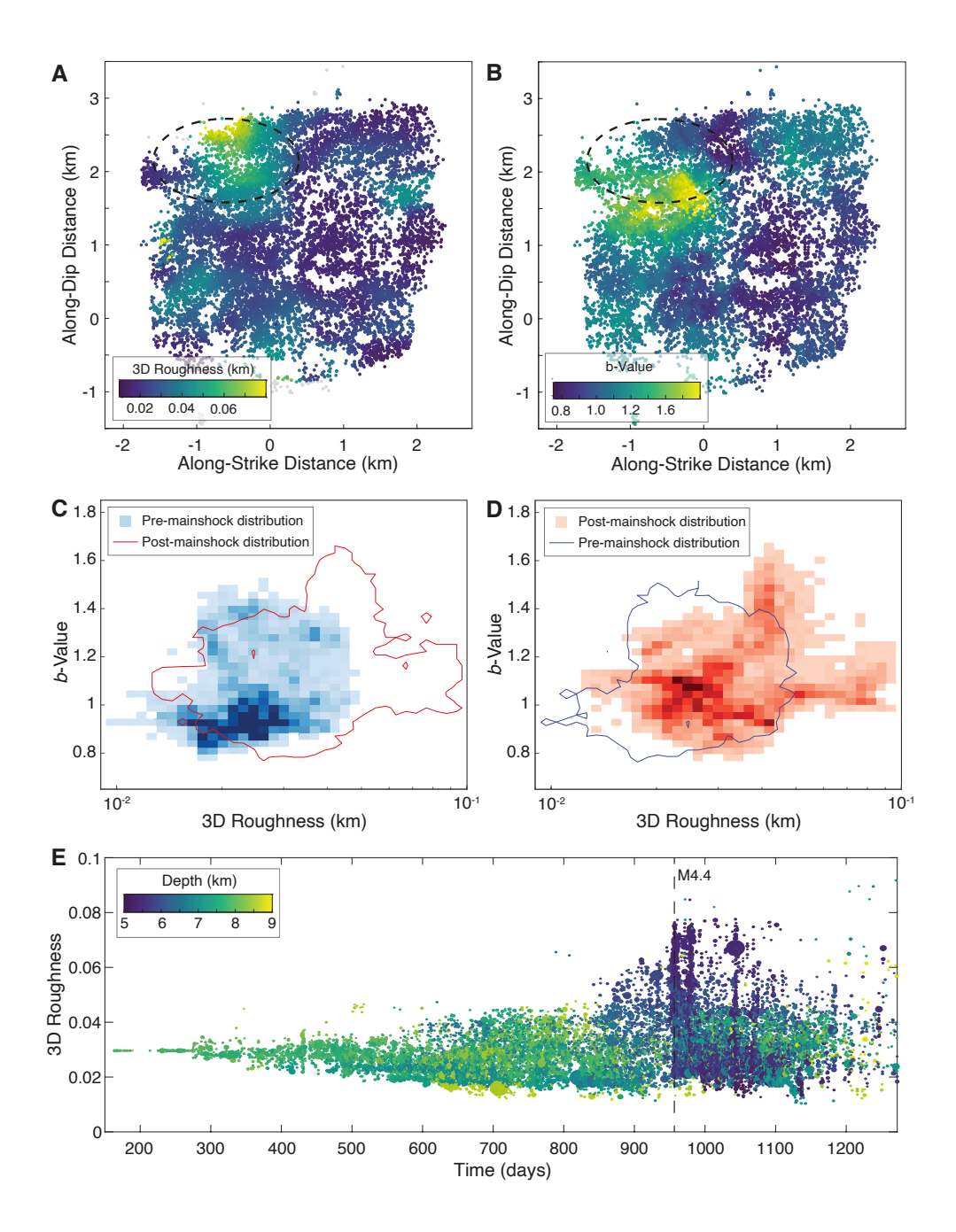


Figure 4. (A) 3D roughness (mean out-of-plane distance, km) estimated at earthquake locations with at least 100 earthquakes within 500 m. (B) b-values estimated at earthquake locations using the 150 closest $M \geq 0.6$ events with positive magnitude differences. (C) Roughness versus b-values estimated for the same event. Shaded blue cells show the distribution of roughness and b-value measurements before the M4.4 earthquake with darker colors representing a higher density of points. Red contour shows the distribution post-M4.4 for comparison. (D) Same as (C), except shaded red cells show the distribution of roughness and b-value after the M4.4 earthquake with darker colors representing a higher density of points. Blue contour shows the distribution pre-M4.4 for comparison. (E) Evolution of 3D roughness as an expanding area of the fault is imaged through time.

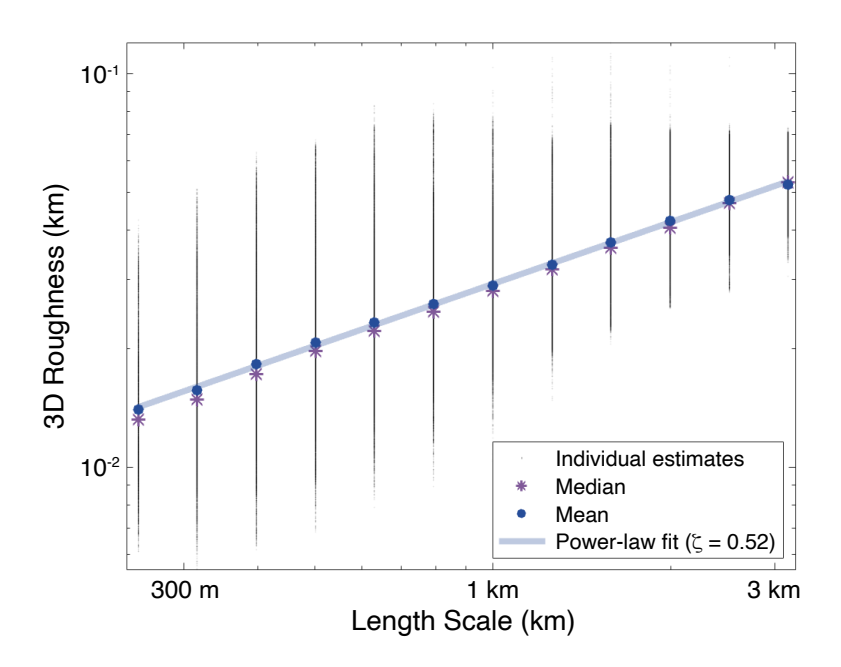


Figure 5. 3D roughness (mean out-of-plane distance, km) estimates for length scales from 250 m to 3 km. Grey points show individual 3D roughness measurements at all earthquake locations with at least 100 points within a given radius (half the length scale). Mean and median values at each length scale are shown by the blue circles and purple asterisks, respectively. The power-law fit (ζ =0.52) to the mean values is shown by the light blue line.